NASA Technical Memorandum 85990

Hover Test of a Full-Scale Hingeless Rotor

William Warmbrodt and Randall L. Peterson

August 1984

NASA

National Aeronautics and
Space Administration

Hover Test of a Full-Scale Hingeless Rotor

William Warmbrodt
Randall L. Peterson, Ames Research Center, Moffett Field, California

NASA

HOVER TEST OF A FULL-SCALE HINGELESS ROTOR

William Warmbrodt and Randall L. Peterson
NASA Ames Research Center, Moffett Field, California 94035, U.S.A.

ABSTRACT

The performance and aeroelastic stability in hover of a 9.8-m-diam, hingeless helicopter rotor system was evaluated. Rotor performance and inplane damping data were obtained for rotor operation between 350 and 425 rpm for thrust coefficients (C_T/σ) between 0.0 and 0.12. At constant rotor thrust, a minimum in rotor inplane damping was measured at 400 rpm; the effect of experimental data scatter on this damping trend was determined to be insignificant. Good agreement is shown between experimental performance data and performance predicted by a comprehensive computer code. The influence of different aerodynamic inflow models on predicting damping levels is also shown. The best correlation with experimental stability data was obtained when a dynamic inflow model was used instead of static or quasi-static inflow models. Direct comparisons were also made between the hingeless rotor data and data from a full-scale, bearingless main rotor test performed on the same general-purpose test apparatus. The aerodynamic efficiency of the bearingless rotor was less at low thrust conditions, but was the same at design thrust. At low-thrust levels the bearingless main rotor was less damped than the hingeless rotor.

NOMENCLATURE

c	blade chord, m
C_P/σ	rotor power coefficient, rotor power$/\rho S(\Omega R)^3$
C_T/σ	rotor thrust coefficient, shaft axes, thrust$/\rho S(\Omega R)^2$
C_ζ	viscous damping of wind-tunnel balance modes, (N·sec)/m
I_θ	rigid-blade pitch inertia about feathering axis, kg·m^2
K_θ	rotor cyclic control system stiffness, N·m/rad
R	rotor radius, m
S	rotor reference area, $4cR$, m^2
ρ	air density, kg/m^3
σ	damping decay coefficient, sec^{-1}; rotor solidity
ω_ζ	rotor-blade fundamental inplane bending frequency, rad/sec

ω_θ nonrotating cyclic control system frequency, per rev at design
        tip speed

Ω rotor rotation frequency, rad/sec

1. INTRODUCTION

Future advances in rotor-hub design hold the promise of major
improvements in rotorcraft performance. Reducing the complexity of and
the number of parts in the rotor-hub system will improve hub aerody-
namics, increase reliability, and reduce maintenance requirements. The
current use of elastomeric bearings has already reduced the complexity
and size of the hubs used in many helicopters. With hingeless and
bearingless hubs, the control power will also be increased over that
of helicopters in which the conventional articulated rotor system is
used. Consequently, it is likely that there will be significant use of
hingeless and bearingless rotor systems in future rotorcraft.

The design of these advanced rotor-hub systems will require
validated analytical codes that can reliably predict rotor performance
and stability. Many experimental studies have been made in which the
emphasis was on evaluating the aeromechanical stability of advanced
rotor-hub systems. In most of that work, however, model-scale rotor
systems were used. As a result, there are still questions about geo-
metric, dynamic, and aerodynamic scaling and fabrication details, and
a need exists for accurately defining the operational characteristics
of full-scale helicopter rotor systems. Once the necessary data are
obtained, they can be used to validate theoretical prediction codes and
to identify areas where current analytical techniques must be further
developed.

This paper presents results from a hover test of a BO-105 heli-
copter rotor system in the 40- by 80-Foot Wind Tunnel test section at
Ames Research Center (fig. 1). Rotor aerodynamic performance and aero-
elastic inplane damping data were obtained for rotor operation between
350 and 425 rpm (design speed), and for rotor thrust coefficients
(C_T/σ) between 0.0 and 0.12. (These test results constitute one of the
relatively few well-documented aeroelastic stability data sets that
exist for full-scale hingeless-rotor systems; see ref. 1 for details.)
A comprehensive rotorcraft computer code (ref. 2) was then used to pre-
dict the rotor hover performance for the same conditions, and the pre-
dictions and experimental data were compared. The sensitivity of pre-
dicted performance to different rotor-wake models was also investigated,
as well as the effects on predicted stability levels of varying the
number of generalized blade-and-body degrees of freedom, of blade struc-
tural damping, and of control-system stiffness.

As reported by various other researchers, the use of an unsteady
aerodynamic model (dynamic inflow) can significantly improve the corre-
lation between predicted and experimental results. The results from an
analytical model without dynamic inflow, with a quasi-static inflow
model, and with a dynamic inflow model are compared with the experi-
mental data. The data presented here are also compared with previously
published damping data for the same rotor system. Those previously
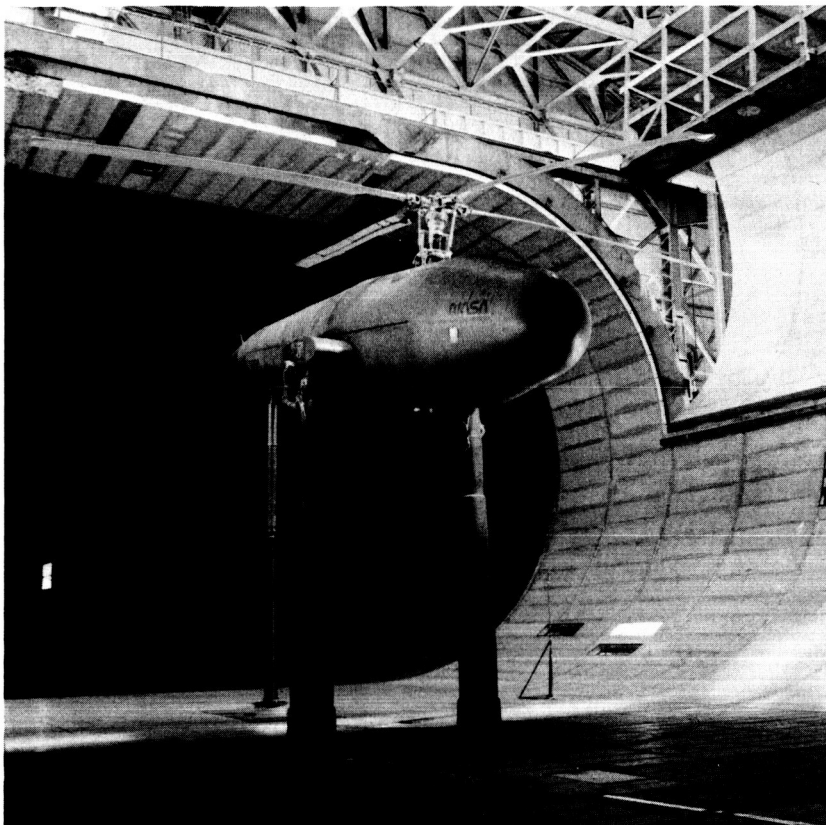
Figure 1. BO-105 rotor system on Ames Rotor Test Apparatus in
40- by 80-Foot Wind Tunnel test section.

reported data (ref. 3) were obtained on a whirl-tower, whereas a wind-
tunnel support system was used in the present study. The new data set
is also used here to make direct comparisons with full-scale, bearing-
less main rotor data obtained on the same wind-tunnel support system
(ref. 4).

2. <u>TEST HARDWARE</u>

The BO-105 helicopter rotor system is a four-bladed, soft inplane
($\omega_\zeta < \Omega$) rotor with constant chord (0.27 m), -8° linear twist, and a
NACA 23012 airfoil. The rotor radius is 4.91 m; rotor solidity (σ) is
0.070. The rotor hub has 2.5° of built-in coning and zero droop or
sweep of the blade outboard of the pitch bearing (fig. 2). The BO-105
rotor used in this test was a production rotor set previously used in
a flight-test program. Additional details about the rotor system are
presented in reference 5. Calculated rotating coupled-bending and
uncoupled-torsion frequencies at the design tip speed of 218 m/sec
(425 rpm) are presented in table 1.

The rotor was installed on the Rotor Test Apparatus at Ames
(fig. 1). This apparatus is a special-purpose drive and support system
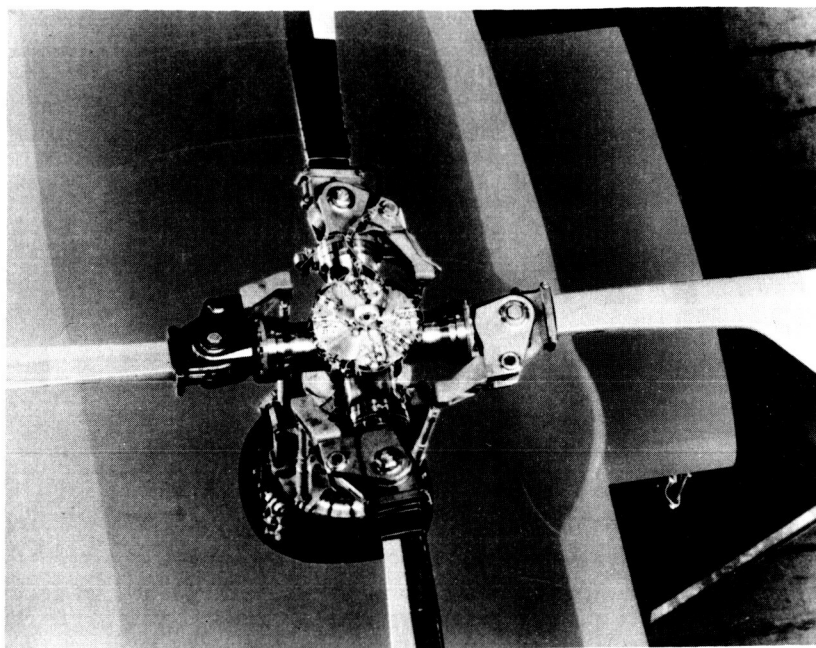for operating helicopter rotors in the 40- by 80-Foot Wind Tunnel. It

Figure 2. BO-105 hingeless-rotor hub.

Table 1.- Calculated rotating blade frequencies (per rev) at 425 rpm

	First mode	Second mode	Third mode
Flapwise	1.10	2.75	4.89
Edgewise	0.73	4.46	11.54
Torsion	3.56	6.48	10.73

houses two electric drive motors, the hydraulic servoactuators of the primary control system, and a dynamic control system capable of introducing dynamic perturbations to the nonrotating swashplate (collective and tilt) at frequencies up to 30 Hz. This system was used during testing to excite the rotor at its fundamental inplane bending frequency for stability measurements.

A shake test was performed before the principal test to determine the dynamic characteristics of the test apparatus and of the balance system with the eight balance dampers engaged. A blades-off hub configuration was used. This test was conducted, in part, to determine any changes in the wind-tunnel balance dynamics owing to recent modifications in its operational configuration. The results are presented in table 2 for both longitudinal and lateral excitation at the hub. Frequency and damping levels for the lowest balance and strut modes are shown. Also shown in table 2 are the results from the most recent previous shake test (1978), performed in a similar manner, before the balance system modification; the support-system frequencies are essentially unchanged, although damping levels are different.

Table 2.- Support-system dynamic characteristics for BO-105
hover test

Direction of excitation	Mode	ω, Hz	C_ζ, N·sec/m	1978 results	
				ω, Hz	C_ζ, N·sec/m
Longitudinal	Balance	2.24	119,600	2.14	88,400
	Strut	4.17	49,160	4.22	43,900
Lateral	Balance	2.71	51,900	2.63	43,800
	Strut	4.64	35,940	4.56	30,600

3. PERFORMANCE TESTING

Hover testing of the BO-105 rotor system was performed with the
wind-tunnel access doors open and with the rotor shaft tilted forward
10° to reduce airflow recirculation (fig. 1). Test conditions were
established by setting the rotor rotation speed and rotor thrust coef-
ficient (C_T/σ). Cyclic pitch was then used to nominally null any once-
per-revolution flapping, as measured using a resolved, flapwise bending-
moment signal from the blade root at station 0.10R. Both longitudinal
and lateral cyclic pitch inputs of the order of ±0.2° were required to
null this once-per-revolution flapping.

4. STABILITY TESTING

A transient decay time-history from an edgewise bending-moment
signal (station 0.10R) was used to determine system stability. The
damping level was determined for only the fundamental edgewise bending
mode. After obtaining the desired operating conditions, the dynamic
control system was used to oscillate the cyclic pitch of the rotor at
the rotor-regressing inplane bending frequency (nutation-type excita-
tion). A chordwise bending-moment signal was monitored, and the ampli-
tude of the oscillation of the swashplate was increased until either an
adequate signal at the forcing frequency was obtained in the blade
chordwise bending moment, or until a load limit was reached at any of
the instrumented blade stations. Abrupt termination of the excitation
yielded the transient decay of the blade edgewise bending-moment signal.
This signal was recorded and analyzed using the moving-block technique.
Several stability records were obtained at each operating condition.
An 8-sec portion of the decaying analog signal was digitized and a
spectral analysis was made. Using an appropriately selected 5-sec por-
tion of the time-history, the transient signal was analyzed using a
one-quarter (or 1.25 sec) block size at the fundamental edgewise bend-
ing frequency.

As mentioned above, excitation of blade chordwise bending motion
was accomplished by oscillating the swashplate at the regressing inplane
modal frequency. Because of this control input, the rotor responded to
blade-pitch motion at the regressing inplane modal frequency in the

rotating system. The resulting transient decay record obtained from the chordwise bending-moment signal consequently yielded the damping information for the regressing inplane mode. Since the progressing inplane mode was not excited, it should not contaminate the transient decay time-history data or the damping determination. This excitation technique is considered superior to either step or impulse inputs to the rotor control system or body modes since it does not require time-histories from each blade (and a subsequent multiblade coordinate transformation) to determine the rotor inplane modal characteristics. It should be noted that this means of rotor-mode excitation could also be used to excite the progressing inplane mode separately, although this was not done in this test. However, analytical results are discussed in this paper to demonstrate that the experimental data are for the regressing inplane mode, which is typically the most important rotor mode for aeromechanical considerations such as ground or air resonance.

5. RESULTS

Rotor Performance Data

Rotor hover performance is shown in figure 3 for rotor speeds of 350, 375, 400, and 425 rpm. The nondimensional power coefficient, C_P/σ, is plotted versus the nondimensional thrust coefficient, C_T/σ, in figure 3a. Rotor figure of merit is shown in figure 3b. As shown in these figures, the influence of rotor rotation rate (tip Mach number) is evident yet small. The minimum power required is obtained at zero thrust conditions.
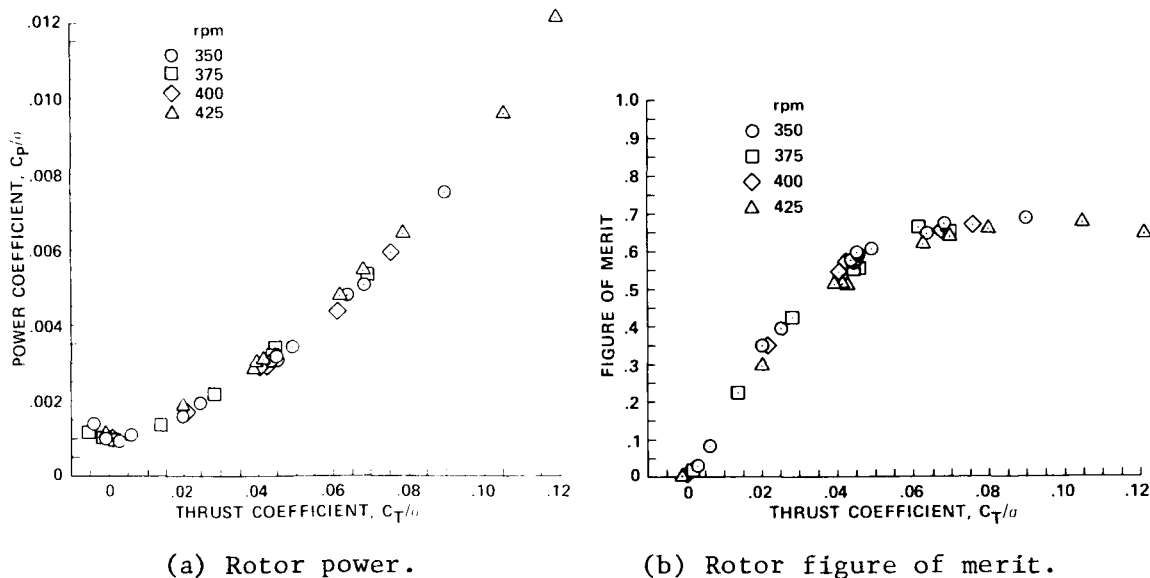

(a) Rotor power. (b) Rotor figure of merit.

Figure 3. Rotor hover performance.

Comparison with analytical predictions made by the computer code, described in reference 2, is shown in figures 4a and 4b. Three different inflow models were used: a uniform inflow model, a prescribed wake

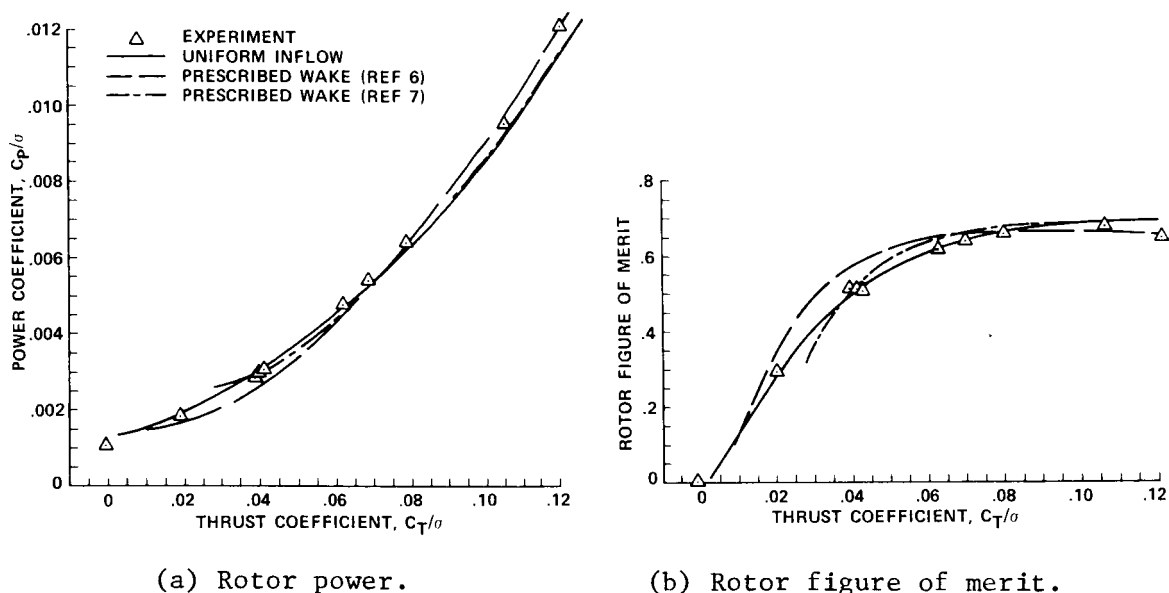(a) Rotor power. (b) Rotor figure of merit.

Figure 4. Predicted rotor performance, 425 rpm.

model based on that of Landgrebe (ref. 6), and a prescribed wake model
based on that of Kocurek and Tangler (ref. 7). Each analysis uses two
elastic-blade bending modes plus a rigid-blade and one elastic-blade
torsion mode. Figure 4a shows the predicted power versus thrust curves
for a rotor speed of 425 rpm. At thrust levels below $C_T/\sigma = 0.06$, the
uniform inflow model correlates well. However, at high thrust levels,
the power required is predicted well with the Landgrebe wake model.
The same data are presented in figure 4b in terms of rotor figure of
merit (FM). For $C_T/\sigma < 0.08$, the uniform inflow model gives the best
correlation. Yet, only the Landgrebe wake model predicts a reduction
in FM at high thrust $(0.10 < C_T/\sigma < 0.12)$. The difference between these
two prescribed wake models for this rotor system is shown in figure 5.
In figure 5a, the nondimensional radial location of the tip vortex
beneath the rotor blade at the first following-blade encounter shows
little difference between the two models. However, the nondimensional
vertical separation distance between the tip vortex and the first fol-
lowing blade (fig. 5b) shows differences of about 15% between the two
models.

The importance of the effect of the vertical location of the
wake tip vortices on performance is further illustrated in figure 6.
In figure 6a, the vertical convection rate (k_2) in the far wake (after
the first following-blade passage) as a function of rotor thrust is
shown for three different prescribed wake models: (1) the Landgrebe
model (ref. 6); (2) the Tangler-Kocurek model (ref. 7); and (3) a modi-
fied prescribed wake model where k_2 was obtained by matching the pre-
dicted rotor performance with the experimental data. For $C_T/\sigma = 0.12$,
the modified value is the same as would be obtained using the model of
reference 6. However, for $0.08 < C_T/\sigma < 0.11$, the modified value is
just slightly greater than the vertical convection rate of reference 7.
For $C_T/\sigma < 0.08$, an intermediate value for k_2 was selected to best
predict the experimental results. The calculated performance using
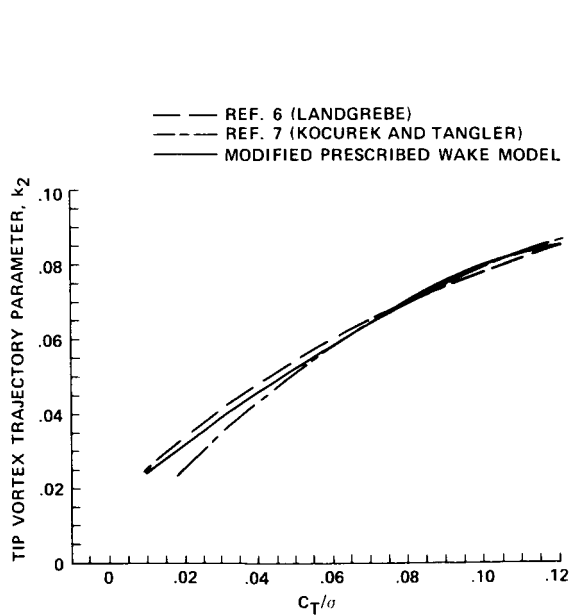this modified wake model is shown in figures 6b and 6c for rotor power
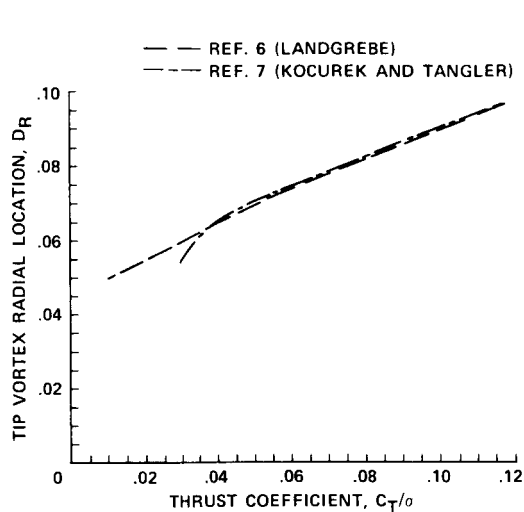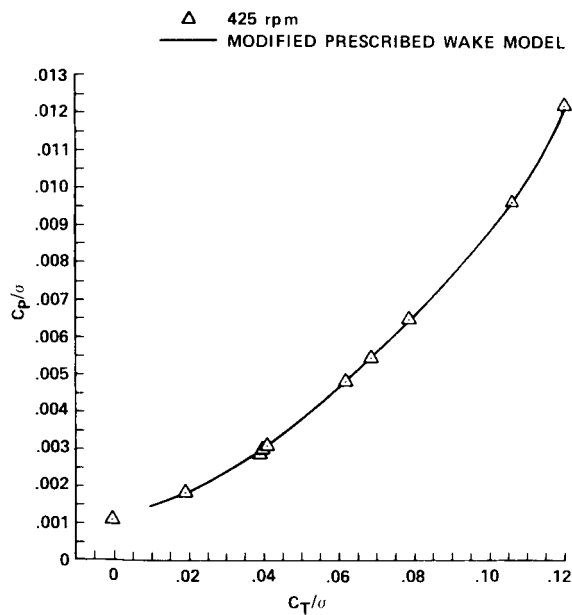
(a) Radial location inboard from blade tip ($\div$ R).
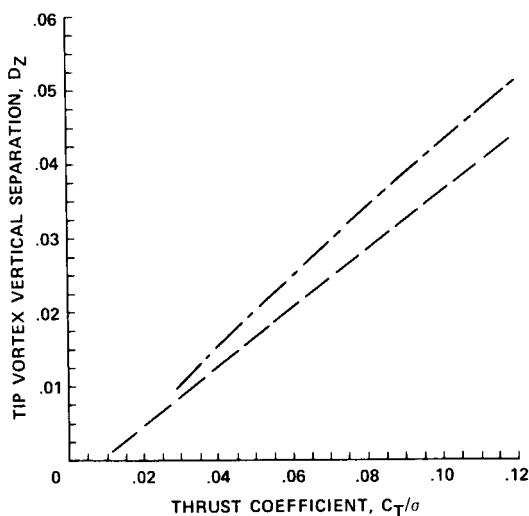
(b) Vertical location below blade ($\div$ R).

Figure 5. Trajectory of prescribed wake tip vortex at first following blade passage.

(a) Axial slope of tip vortex trajectory after first blade passage.
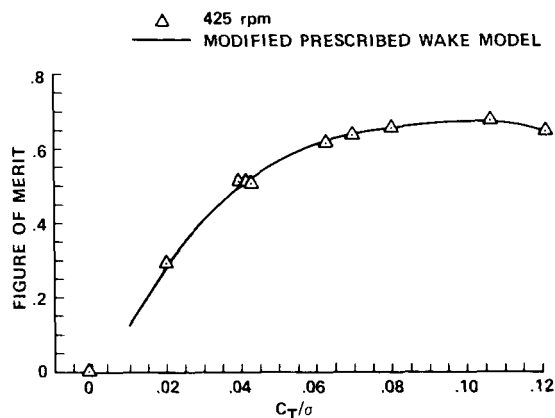
(b) Rotor power.

Figure 6. Predicted aerodynamic performance with modified prescribed wake model: 425 rpm.

and rotor figure of merit, respec-
tively. These results were
obtained using the other rotor-
wake parameters as calculated by
reference 6. Despite only a
slight change to the vertical
location of the tip vortices in
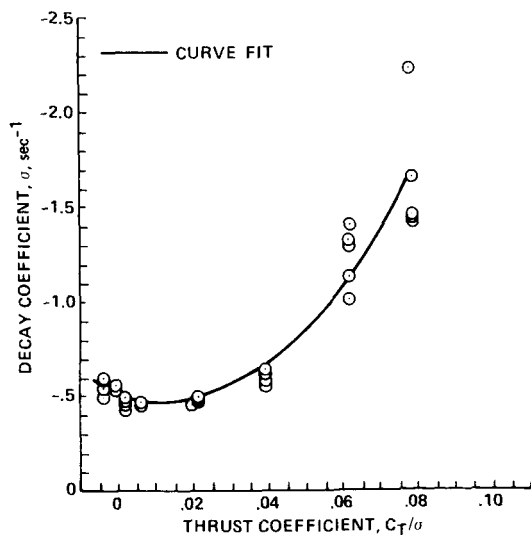the far wake, good correlation is
obtained.

(c) Rotor figure of merit.

Figure 6. Concluded.

Rotor Stability Data

Stability data for all
rotor rotational speeds tested
are shown in figures 7a–7d as a
function of rotor thrust coeffi-
cient (for rotor speeds of 350,
375, 400, and 425 rpm). Each
plotted point is for a unique data record. Scatter in the experimen-
tally determined decay coefficients is small, particularly at lower
damping levels. For each rotor speed, damping is greatest at high
rotor thrust and decreases with reducing thrust. Minimums in modal
damping exist for thrust coefficients between 0.01 and 0.02. As thrust
is further reduced below 0.01, the damping increases. The curves in
figures 7a–7d are second-order, least-squares polynomial regression
curves for the experimental data.

Using the polynomial curve fits from figure 7, damping trends
with constant rotor thrust and changing rotor speed are summarized in
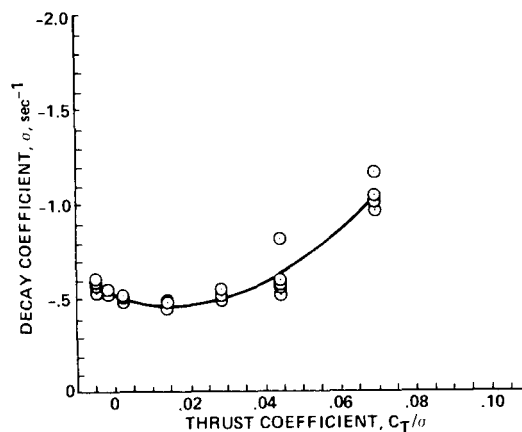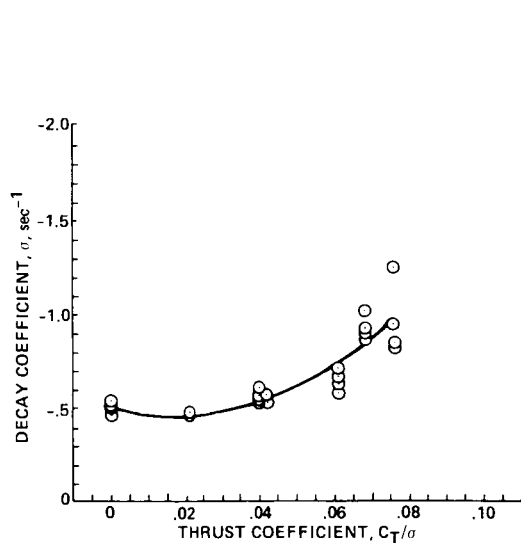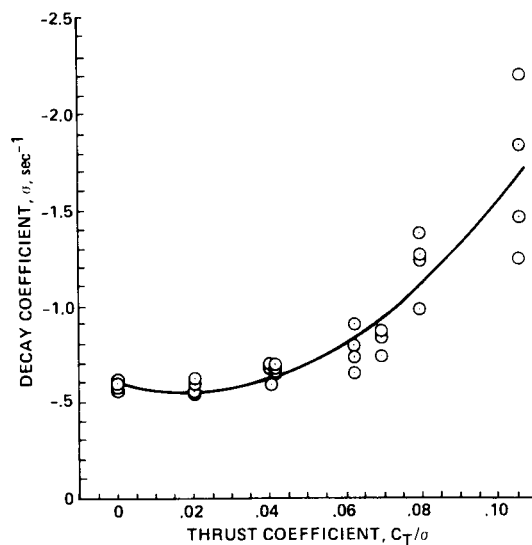

(a) 350 rpm.

(b) 375 rpm.

Figure 7. Rotor regressing inplane modal damping data with polynomial
curve fit.

(c) 400 rpm.

(d) 425 rpm.
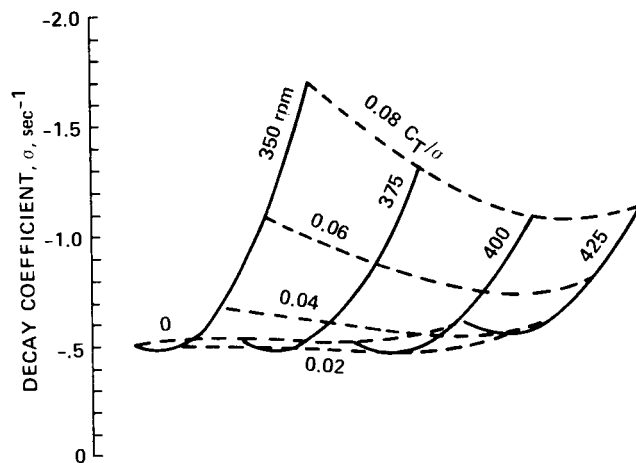
Figure 7. Concluded.

Figure 8. Summary of experimental
hover stability data.

figure 8. The significance
in using a curve fit of the
experimental data to evaluate
trends at constant thrust is
discussed in detail below.
Constant rotor thrust con-
tours (C_T = 0.0, 0.02, 0.04,
0.06, 0.08) are shown. At
constant rotor thrust for
$C_T/\sigma \geq 0.04$, damping reduces
with increasing rotational
speed from 350 to 400 rpm.
This decrease in damping is
judged to be greater than any
uncertainty in damping trends
owing to experimental data
scatter. For low-thrust con-
ditions, $0.0 \leq C_T/\sigma < 0.04$,
little sensitivity to rota-
tion rate is observed between
350 and 400 rpm. At 425 rpm,
however, damping levels
increase for all thrust con-
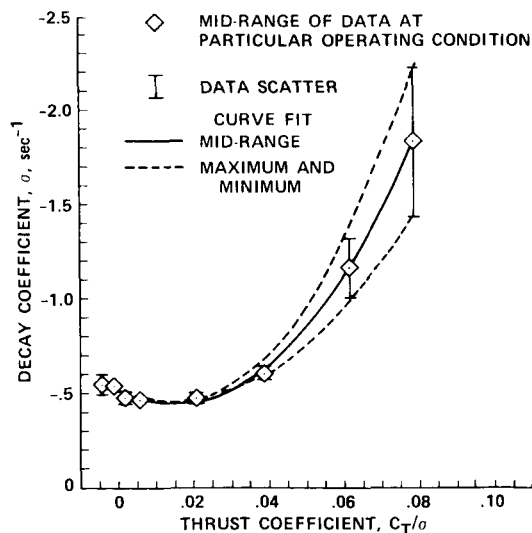ditions. The increased damp-
ing is likely a result of the effects of rotation speed on the complex
structural, inertial, and aerodynamic couplings of the rotor blade.
Another possible explanation for this trend is that system damping is
reduced at 400 rpm because of a ground resonance condition. At 400 rpm,
the measured inplane regressing modal frequency ($\Omega - \omega_\zeta$) is in resonance
with the longitudinal balance mode at 2.24 Hz (table 1). This resonant
operating condition is clearly shown in figure 9. The two lowest
frequency-balance modal frequencies determined from the shake test are

plotted. The experimentally mea-
sured inplane frequency ω_ζ was
used to calculate the regressing
inplane modal frequency $(\Omega - \omega_\zeta)$.
Consequently, the reduced
regressing inplane modal damp-
ing at higher thrust levels,
$C_T/\sigma \geq 0.04$ (fig. 7), and at
400 rpm could be due to a
resonant operating condition.
This is, however, not supported
by analytical results (discussed
later). As mentioned previously,
the increase in damping at
$C_T/\sigma = 0.0$ relative to
$C_T/\sigma = 0.02$ is clearly seen
for each rotational speed.

Figure 9. Inplane regressing modal
frequency as a function of rotor
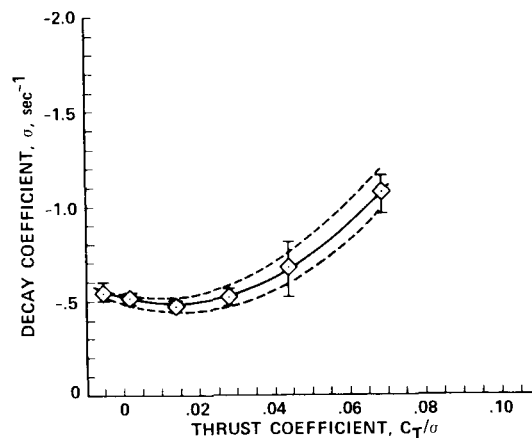rotational speed ($C_T/\sigma = 0.07$).
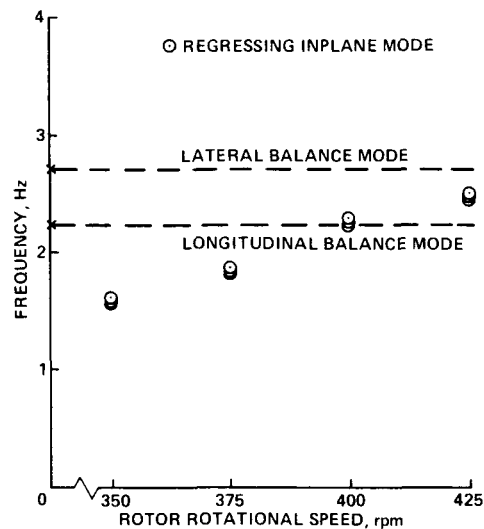
As part of this study, an
attempt was made to evaluate the
significance of using polynomial
curve fits to the experimental
data (fig. 7) to investigate damping trends with rotor thrust and rota-
tion rate (fig. 8). In doing so, an estimate of the effects of data
scatter on measured damping levels and resultant trends can be more
closely reviewed. This is important in understanding the effect of
experimental data scatter on observed damping trends and has not been
thoroughly addressed in previous studies. In figures 10a-10d, the
plotted data points are the midpoints of the data range at that par-
ticular thrust condition for rotor speeds of 350, 375, 400, and 425 rpm.
The vertical bars show the range of data scatter at these thrust

(a) 350 rpm.

(b) 375 rpm.

Figure 10. Polynomial curve fit of (max-min)/2 regressing inplane modal
damping data at each operating condition.
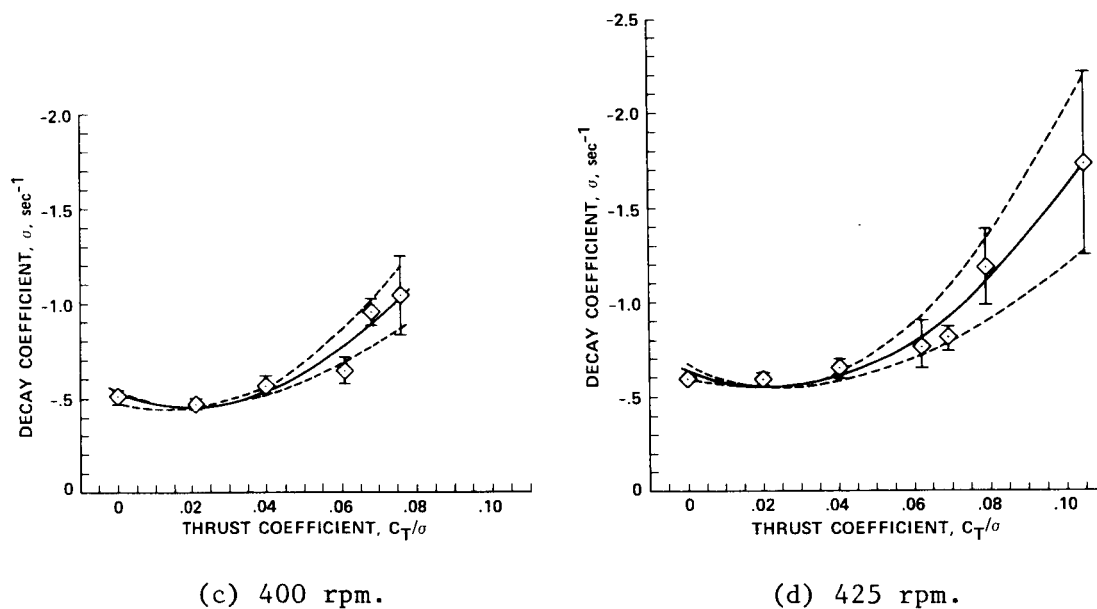
(c) 400 rpm.

(d) 425 rpm.

Figure 10. Concluded.

conditions. The solid curves are again second-order, least-squares
polynomial regression curves for these mid-range data and the dashed
curves are for the maximum and minimum extrema. A somewhat different
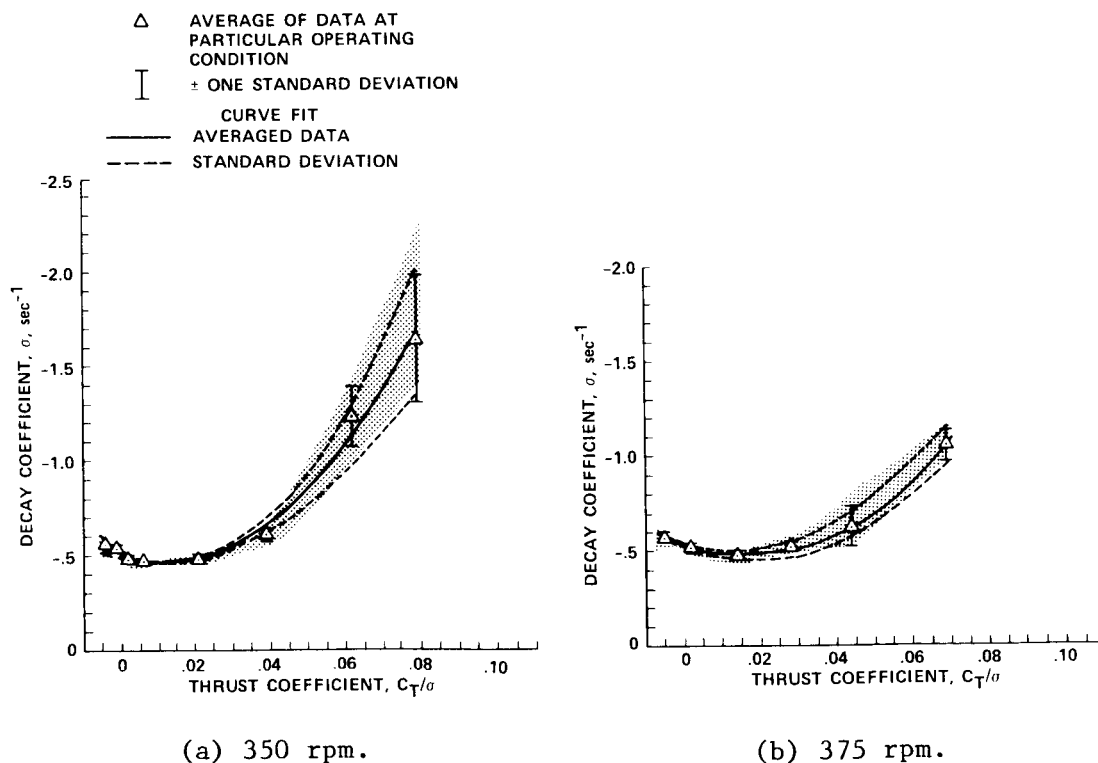set of values is shown in figures 11a-11d where the plotted data point

(a) 350 rpm.

(b) 375 rpm.

Figure 11. Polynomial curve fit of average regressing inplane modal
damping data at each operating condition.
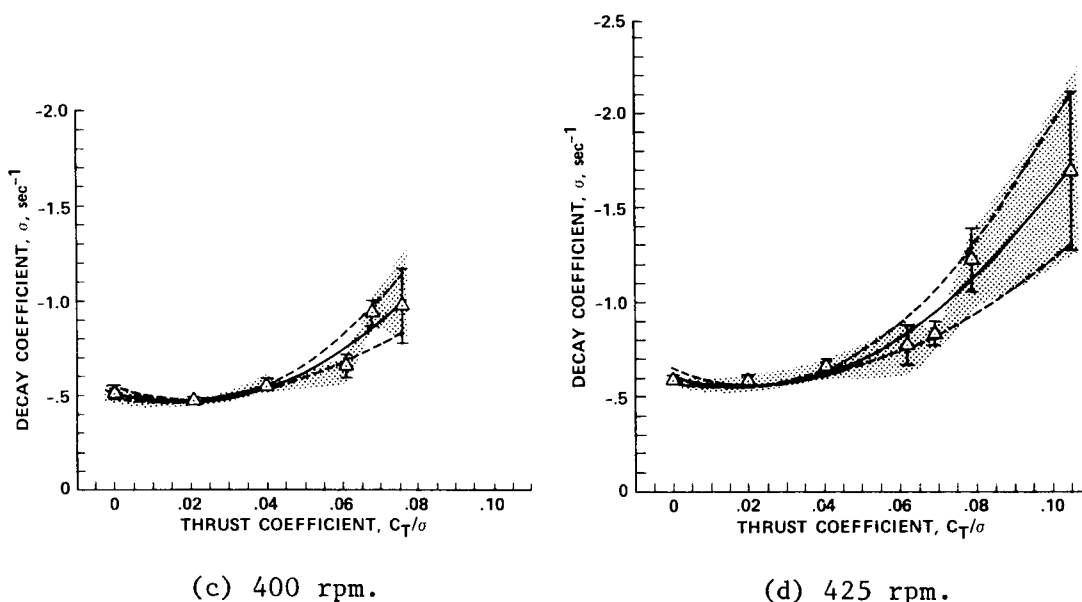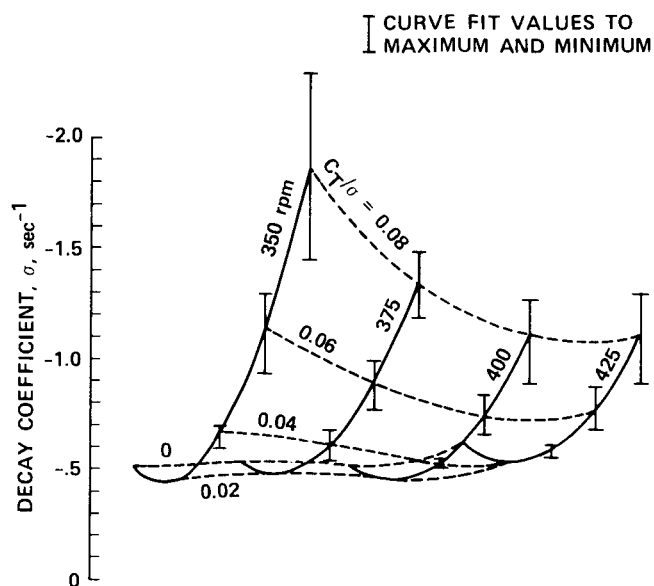
(c) 400 rpm.

(d) 425 rpm.
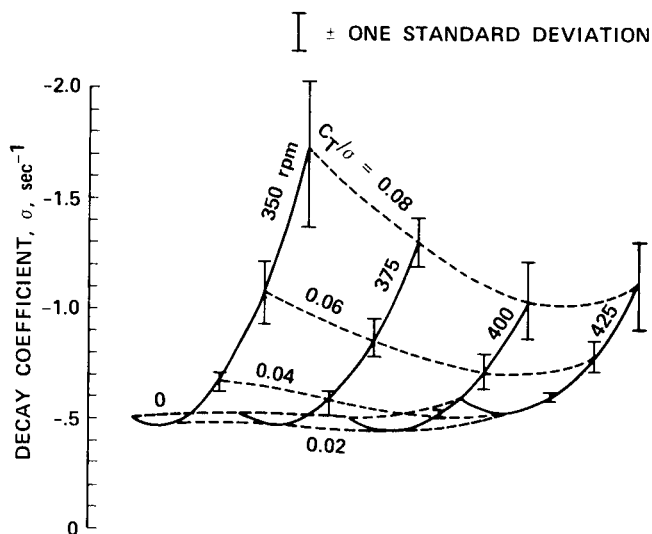
Figure 11. Concluded.

at each operating condition is the average value calculated from all of
the data at that particular thrust. The shaded area shows the range of
experimentally determined decay coefficients. The vertical bars in
figure 11 are plus or minus one standard deviation determined from
these data. Again the curves are second-order regression curves of
these average data.

Using the curve fits of figures 10 and 11, damping trends with
constant rotor thrust and changing rotor speed are determined. In
figure 12a, the resulting curves from the mid-range data (fig. 10) are
used, and in figure 12b, the resulting curves from the averaged data
(fig. 12) are used. The vertical bars in figure 12a are the polynomial
curve fits to the extrema of the data scatter at $C_T/\sigma = 0.04$, 0.06,
and 0.08. The vertical bars in figure 12b are polynomial curve-fits
for one standard deviation at $C_T/\sigma = 0.04$, 0.06, and 0.08 (fig. 11).
Figures 12a and 12b can be directly compared with figure 8 to determine
the influence of experimental data scatter on the damping trends at
constant thrust with increasing rotor rotation rate. Recall that fig-
ure 8 was obtained using curves (fig. 7) obtained by using a regression
analysis with each damping determination considered separately. Several
observations can be made. At 350 rpm, the midpoint data curve (fig. 12a)
shows higher damping at $C_T/\sigma = 0.08$ and lower damping at $C_T/\sigma = 0.02$
than the other figures. However, all three curves (and consequently all
three ways of accounting for data scatter) show the same two major trends
with constant thrust: (1) at high thrust coefficients ($C_T/\sigma > 0.04$)
reduction in damping with increasing rotor speed to a minimum at 400 rpm;
and (2) minimum damping for all rotor speeds between $0.0 < C_T/\sigma < 0.02$.
These results are considered further in the discussion of the correlation
of experimental data and analytical predictions.

The conclusions that may be drawn from these figures are impor-
tant. The level of damping-data scatter from this experiment is

68-13

CURVE FIT VALUES TO MAXIMUM AND MINIMUM

(graph, part a — decay coefficient vs operating conditions)

DECAY COEFFICIENT, σ, sec^{-1}

-2.0, -1.5, -1.0, -.5, 0

350 rpm, 375, 400, 425

$C_T/\sigma = 0.08$, 0.06, 0.04, 0.02, 0

(a) (Max-min)/2 data (fig. 10).

$\pm$ ONE STANDARD DEVIATION

(graph, part b)

DECAY COEFFICIENT, σ, sec^{-1}

-2.0, -1.5, -1.0, -.5, 0

350 rpm, 375, 400, 425

$C_T/\sigma = 0.08$, 0.06, 0.04, 0.02, 0

(b) Averaged data at each operating condition (fig. 11).

Figure 12. Summary of curve fit regressing inplane modal damping data.

representative of good quality stability data obtained in a number of other experiments. When the system is lightly damped, good quality transient decay records can be obtained, and the resulting measured damping values are very repeatable. For a number of reasons, greater scatter is obtained at highly damped conditions; for example, because of difficulty in exciting the mode, a short-duration transient, and a poor single-degree-of-freedom decay curve fit. However, given the inherent limitations of the test procedures and the resulting data-scatter bands, it is concluded that the important trends are evident despite what may appear to be significant data scatter for some high-thrust operating conditions.

Correlation of stability data with analytical prediction (ref. 2) is shown in figures 13-17. The definition of rotor properties was taken from reference 5. The shaded area identifies the range of experimental damping values shown in figure 7. Because a four-bladed rotor was used in the hover operating condition, only cyclic rotor modes for elastic-blade bending and rigid and elastic torsion deflections were modeled in the analysis. The collective and reactionless rotor modes were not modeled, a result of the lack of coupling with other rotor and support system modes. As discussed in detail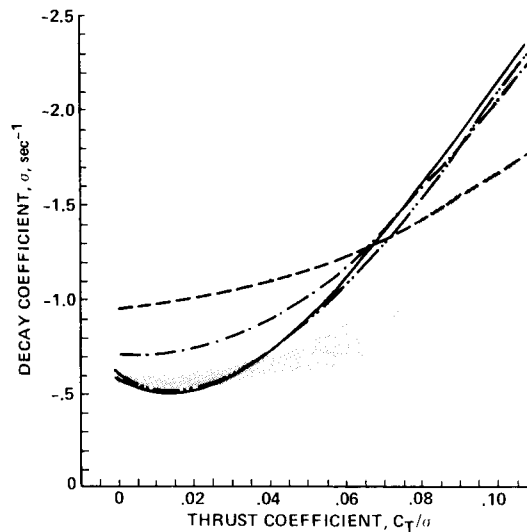 in reference 8, a structural damping value of 0.03 is used in all the results here. Likewise, two support-system degrees of freedom, the first-balance longitudinal mode and first-balance lateral mode (table 2), were modeled in the analysis. Using from zero to six support degrees of freedom in the analysis did not significantly influence the predicted decay coefficients of the inplane modes. Consequently, as discussed in the previous section, resonant operating conditions between the regressing inplane modal
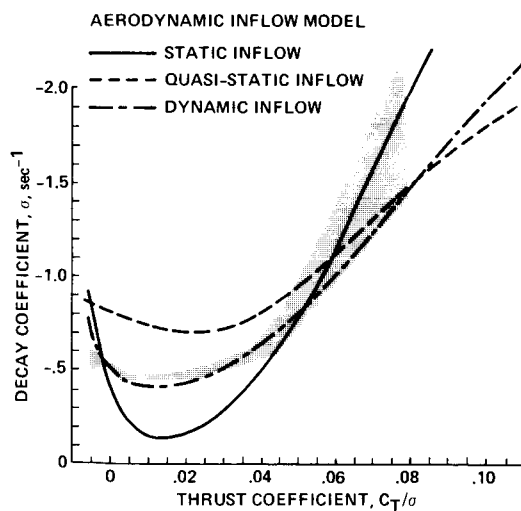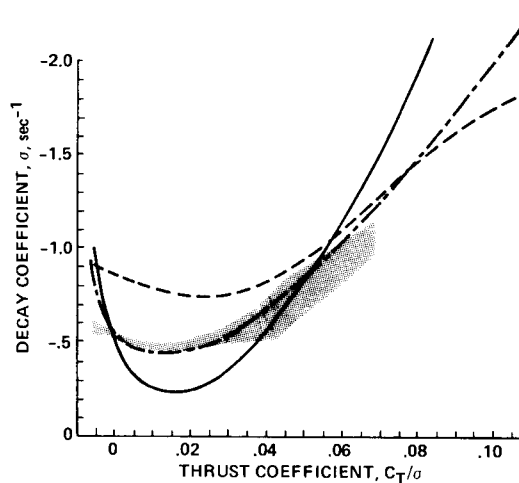
(a) Static inflow model.   (b) Dynamic inflow model.

Figure 13. Effect of number of rotor-blade modes on predicted damping
levels: 425 rpm.

(a) 350 rpm.   (b) 375 rpm.

Figure 14. Effect of different inflow models on predicted damping levels.

frequency and the wind-tunnel balance londitudinal mode at 400 rpm may
not be responsible for the apparent minimum in damping observed in fig-
ure 7. Rather, the increase in damping for constant C_T/σ at 425 rpm
could be interpreted as resulting from aeromechanical coupling between
rotor blade modes.

The influence of using various numbers of rotor modes in the
aeroelastic stability analysis of reference 2 is shown in figure 13 for
a rotor speed of 425 rpm. A baseline cyclic rotor control-system stiff-
ness yielding a nonrotating, $\omega_\theta = 7.3$, rigid torsion modal frequency was
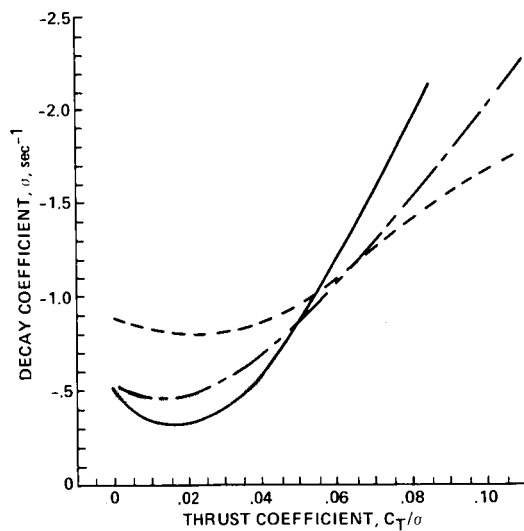
(c) 400 rpm.
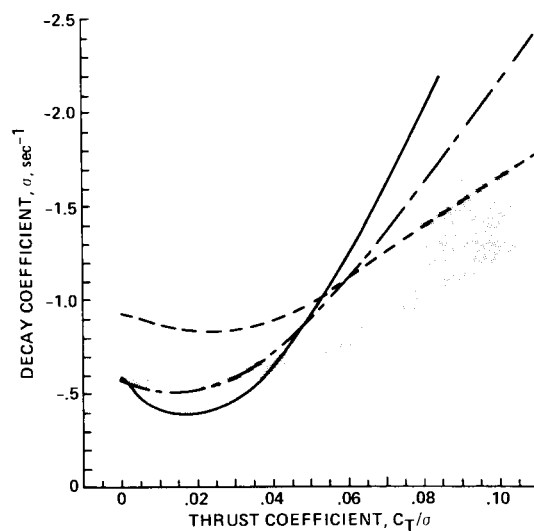
(d) 425 rpm.

Figure 14. Concluded.
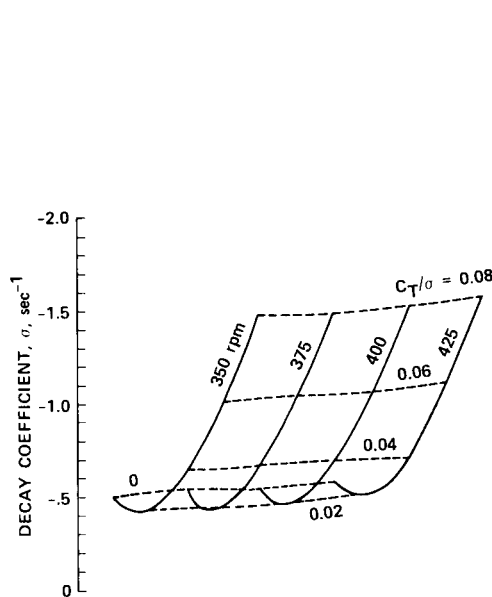
Figure 15. Predicted damping as a function of rotor rotation rate and thrust: dynamic inflow model.
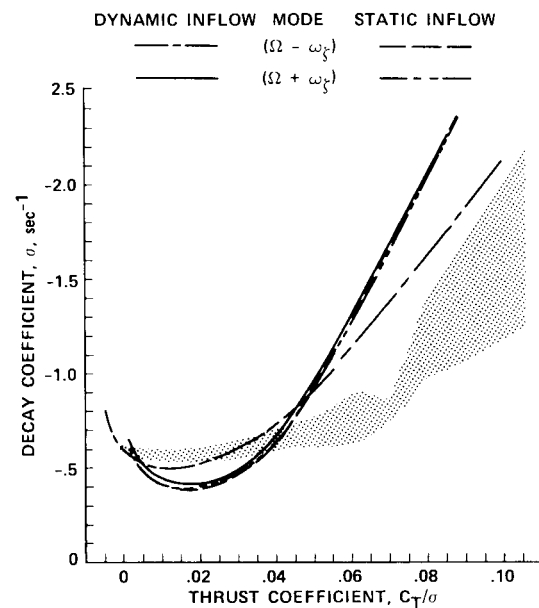
Figure 16. Regressing and progressing inplane modal damping with different aerodynamic inflow models: 425 rpm.

used. In figure 13a, a static inflow aerodynamic model was used, and in figure 13b a dynamic inflow aerodynamic model was used. Results for different numbers of bending and torsion rotor modes are shown. For the static inflow aerodynamic model (fig. 13a) and when only rotor bending is modeled (fundamental flap and lead-lag modes), the predicted damping exceeds the experimentally measured damping data. Introducing a rigid

cyclic torsion mode reduces damp-
ing for $C_T/\sigma \leq 0.06$ and causes
a minimum decay coefficient to be
obtained at $C_T/\sigma = 0.012$.
Including the first elastic tor-
sion mode further reduces the
regressing inplane modal damping
significantly. Additionally,
modeling the second flap and
lead-lag cyclic bending modes
is shown to have little influ-
ence on the predicted results.
Similar results are shown in
figure 13b for the analysis with
a dynamic inflow aerodynamic
model. In this case, excluding
all torsion modes shows less
damping sensitivity to increas-
ing thrust for the predicted
decay coefficients than when
using the static inflow model.
When comparing static inflow and
dynamic inflow results, the
influence of dynamic inflow on
the flap-lag blade model is to reduce the predicted decay coefficient
for all thrust levels. For the full flap-lag-torsion model, dynamic
inflow increases rotor damping for $C_T/\sigma < 0.05$, but decreases rotor
damping for higher thrust levels. In the remaining analytical results
presented in this paper, a rotor model with two elastic-blade bending
modes and two torsion modes (one rigid, one elastic) is used.

Figure 17. Effect of rotor cyclic
control system frequency ω_θ on
predicted damping levels:
425 rpm, dynamic inflow model.

The influence of different aerodynamic models is illustrated in
figure 14. Results are shown for rotor speeds of 350, 375, 400, and
425 rpm, with a static aerodynamic inflow model, a quasi-static aero-
dynamic model, and a dynamic inflow model. Again, a baseline cyclic
rotor control-system nonrotating frequency of $\omega_\theta = 7.3$ was modeled.
The static inflow model underpredicts damping for $C_T/\sigma < 0.05$ for all
rotor rotation speeds and overpredicts damping for $C_T/\sigma > 0.05$ for all
rotor rotation speeds except 350 rpm. The quasi-static inflow model is
less sensitive to thrust variations and gives better agreement with
experimental data than the static inflow model. However, this model
significantly overpredicts damping for $C_T/\sigma < 0.05$. The correlation
obtained with the dynamic inflow model is very good, although at higher
rotor rotational speeds and thrust coefficients, predicted damping
levels exceed measured values. With the dynamic inflow model, the mini-
mum damping level for $0.01 \leq C_T/\sigma \leq 0.02$ is predicted. Although all
three analyses predict significant increases in damping at negative
thrust conditions, insufficient experimental data exist to verify this
trend.

From figure 14, it is seen that all three aerodynamic models fail
to predict the reduction in damping at constant moderate-to-high thrust
levels, $C_T/\sigma \geq 0.04$, for 350 to 400 rpm. This is shown in figure 15,
where the predicted results (with a dynamic inflow model only) as a
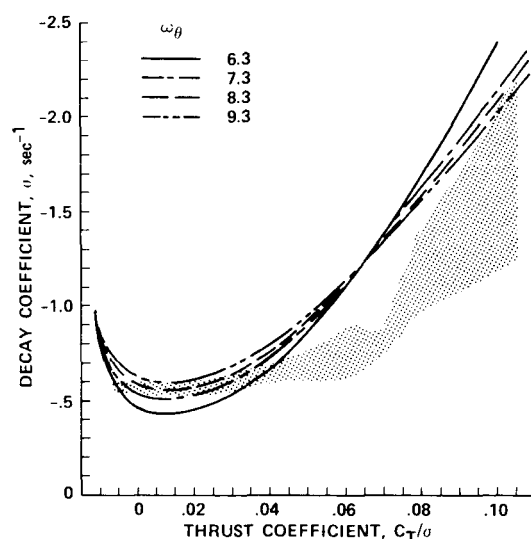function of rotor speed and thrust are presented. From these results,

increasing rotation speed at constant thrust always increases the decay coefficient. Comparing with the curve-fit experimental results of figures 7, 12a, and 12b, it is apparent that minimum damping measured at 400 rpm is not predicted by the analysis. Further study is required to determine the reason for this discrepancy between predicted and measured damping trends.

As discussed in the previous section, the test technique used in this experiment allows for determination of the regressing inplane modal characteristics. To validate this procedure, calculations were performed comparing the decay coefficients with the static aerodynamic inflow model and the dynamic inflow model for both the regressing and progressing inplane modes at 425 rpm (fig. 16). For the static inflow model, each mode has virtually the same decay coefficients, because there is little coupling with the body degrees of freedom, and there is no unsteady wake model to couple with individual rotor modes. Using a dynamic inflow model significantly reduces the inplane regressing mode damping, and the inplane progressing mode damping is almost identical to the decay coefficients obtained for the static inflow model. Dynamic inflow has little or no effect on the progressing inplane mode, a result of this inflow model being a low-frequency, unsteady aerodynamics representation. Because of the high degree of correlation between the predicted damping for the regressing inplane mode using a dynamic inflow model and the experimental data, and because of the poor correlation between experiment and the predicted progressing inplane modal damping, it is apparent that the test technique did successfully allow for direct measurement of the inplane regressing mode characteristics when only recording data from one blade. This test technique, involving individual excitation of inplane rotor modes, will be investigated further in future full-scale rotor dynamic tests.

The influence of the cyclic rotor control-system mode on predicted damping levels at 425 rpm is shown in figure 17. A dynamic inflow model is used for the analysis. Nonrotating frequencies between $6.3 \leq \omega_\theta \leq 9.3$ are shown. The corresponding rotor cyclic control-system stiffness is given in table 3. The baseline value used in obtaining the results shown in figures 13-16 is $\omega_\theta = 7.3$. Although the cyclic control-system stiffness has only moderate influence in reducing damping at high thrust levels, increasing the stiffness can increase the damping at low thrust levels (over 80% for the minimum damping value at $C_T/\sigma = 0.02$). The same trend is obtained when using a static inflow model (ref. 8). Because of the lack of experimental data for the wind-tunnel test configuration, a value of $\omega_\theta = 7.3$ was selected as the baseline value for the results presented in this paper. This results in a rotor test apparatus control-system stiffness that is approximately the same as that of the rotor when it is installed on a BO-105 flight aircraft; the stiffness is also equal to that of other

Table 3.- Control-system stiffness variations used in figure 17: 425 rpm, $I_\theta = 0.106$ kg·m²

ω_θ, 1/rev	ω_θ, rad/sec	K_θ, N·m/rad
6.3	280.4	8,300
7.3	324.9	11,140
8.3	369.4	14,410
9.3	413.9	18,090

similar rotor control systems previously tested on the Ames Rotor Test Apparatus.

6. FULL-SCALE DATA CORRELATION

The wind-tunnel hover performance data for 425-rpm operation is compared with a limited amount of actual flight-test data (acquired in hovering flight) in figure 18. Also shown is the predicted hover performance from the modified prescribed wake model (fig. 6). The flight-test data, obtained from an MBB test program, is limited to the design hover thrust condition of approximately $C_T/\sigma = 0.07$. Since the flight-test data have higher power requirements than the wind-tunnel data, it can be assumed that the additional 10% in rotor thrust is, in part, overcoming the aerodynamic download on the helicopter fuselage and other adverse aerodynamic interactions.

Although few good-quality stability data have been published for full-scale hingeless rotor systems, data do exist for the BO-105 rotor system tested on a whirl tower (ref. 3). These data are compared with the present results in figure 19. The damping data have been presented in terms of percent critical damping in the rotating system. Only 425-rpm whirl-tower data are available for comparison. The whirl-tower data obtained for the lead-lag motion compare well for low rotor thrust ($C_T/\sigma < 0.03$). At moderate rotor thrust levels ($0.05 < C_T/\sigma < 0.08$), the whirl-tower data indicate somewhat higher damping levels. No data for high rotor thrust ($C_T/\sigma > 0.08$) are available for comparison. The predicted damping levels using a dynamic inflow model (fig. 14d) are also shown.
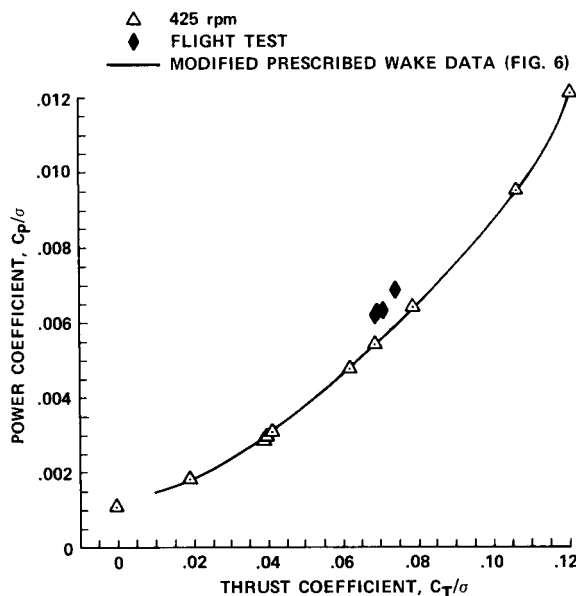

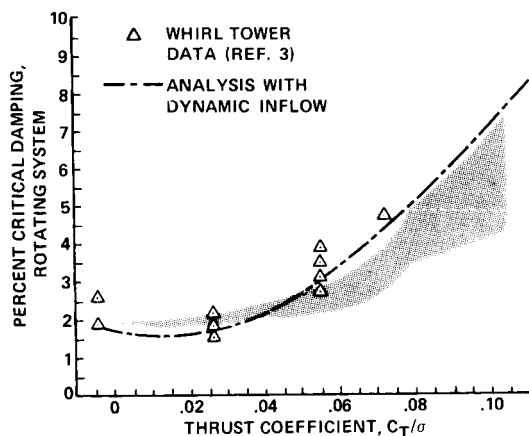Figure 18. Comparison of wind-tunnel and flight-test hover performance data.

Figure 19. Comparison of BO-105 damping data with whirl-tower results.

8. COMPARISON WITH BEARINGLESS MAIN ROTOR DATA

The experimental performance and stability results presented in figures 3 and 7 can be directly compared with those obtained for a bearingless main rotor tested on the same wind-tunnel support system (ref. 4). For the bearingless main rotor, a modified BO-105 rotor system was used in which the hingeless-blade retention system was replaced with a twin-beam flexure/torque-tube assembly. The bearingless root-retention system used elastic deformation to allow for blade-pitch angle control. The results presented here are important because the bearingless rotor was designed and built to have characteristics similar to those of the BO-105 rotor system. Outboard of the blade-retention clevis, the rotor blades in the two rotor systems are identical. Consequently, differences in performance and damping trends can only be attributed to the flexure retention system of the bearingless main rotor. It is important to note that the support-system dynamics, as shown in table 2, were essentially unchanged between the two tests.
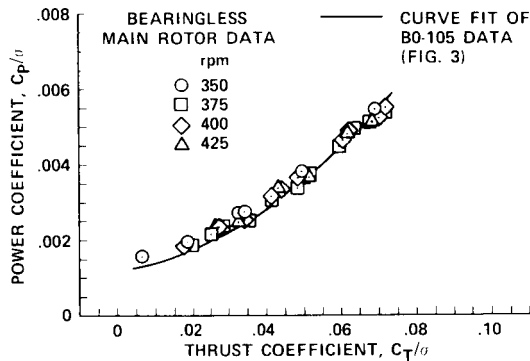

Figure 20. Comparison of BO-105 and bearingless main-rotor performance data.

In figure 20, bearingless main-rotor performance data are plotted with a polynomial curve fitted to the BO-105 performance data taken from figure 3. In both data sets, bare hub tares (without flexbeam assemblies for the bearingless rotor) have been subtracted. Because of the large blade clevises located at the outboard end of the flexbeams and the unfaired flexbeam/torque-tube assemblies, the bearingless main rotor is expected to show, and indeed does show, poorer performance for thrust coefficients below 0.06. Above this value, the performance of the two rotor systems is comparable. This could be explained by the wake of the bearingless main rotor inducing less body download on the test apparatus than did that of the BO-105 rotor system.

Figure 21 shows the damping data comparison for rotor speeds of 350, 375, 400, and 425 rpm. At 375 and 400 rpm, the data from the two rotor systems are very similar. At design 1-g operating speed, 425 rpm, the bearingless main rotor is more stable than the BO-105 rotor at a nominal hover thrust condition of $C_T/\sigma = 0.068$. However, the bearingless main-rotor damping level becomes lower than that of the BO-105 as rotor thrust is reduced. At 350 rpm, the different damping levels of the two rotor systems are more pronounced, the bearingless main rotor being significantly less damped, particularly at very low thrust conditions.

□ BEARINGLESS MAIN ROTOR
DATA (REF. 4)

(a) 350 rpm.

(b) 375 rpm.

(c) 400 rpm.

(d) 425 rpm.
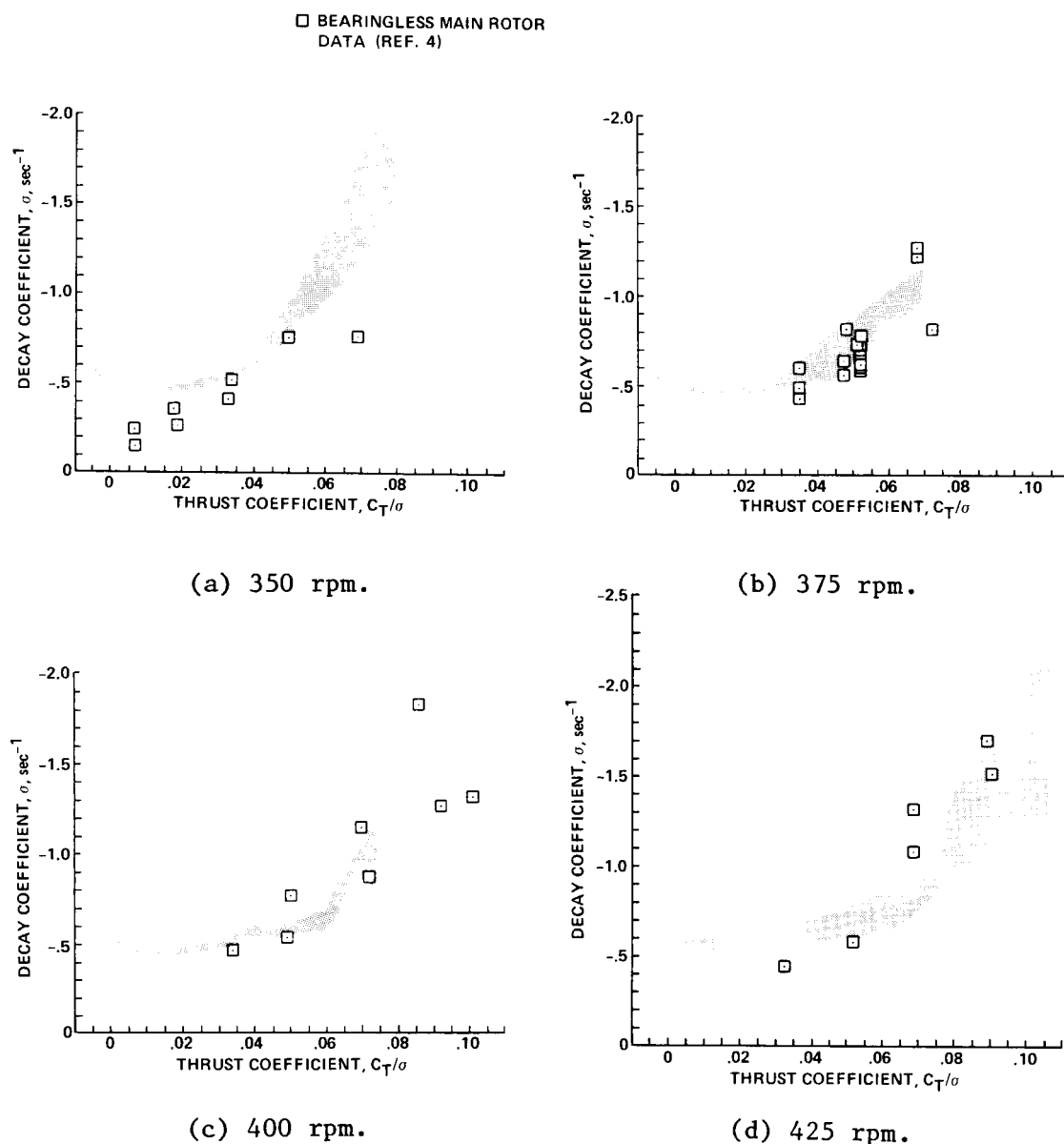
Figure 21.   Comparison of BO-105 and bearingless main-rotor damping data.

9.   CONCLUSIONS

A full-scale, BO-105 helicopter hingeless-rotor system was tested
in hover. Performance and damping of the regressing inplane rotor mode
was determined for trends with changing rotor thrust and tip speed.
These experimental data have been compared with analytical predictions
and other hover data. Direct comparison between results for a bearing-
less main-rotor system and the BO-105 rotor are presented. The major
findings of this study are as follows:

1. BO-105 rotor-system damping varies with rotor thrust at constant rotational speed. A minimum damping level is obtained at a C_T/σ of about 0.02. At constant thrust ($C_T/\sigma \geq 0.02$), the rotor system is least stable at 400 rpm.

2. Experimental damping data scatter, although significant for highly damped rotor operating conditions, did not limit the determination of damping trends with varying rotor rotation speed at constant thrust.

3. Predicted aerodynamic performance using a modified prescribed wake model for the location of the tip vortices in the far wake adequately predicted rotor power and figure of merit as functions of thrust.

4. Damping trends at constant rotor speed are well predicted with a comprehensive rotorcraft analysis. Although the predicted results were not sensitive to the number of support-system modes modeled, the first two elastic-blade bending modes and the first rigid-blade and elastic-blade torsion modes of the blades were required for adequate correlation.

5. Neither minimum damping levels nor damping trends with varying thrust at constant rotation speed for the regressing inplane mode are accurately predicted using a static or a quasi-static inflow model. A dynamic inflow model significantly improves the correlation between predicted and experimental performance at all thrust conditions. However, reduction in damping at moderate constant-thrust conditions when increasing rotor rotation speed from 350 to 400 rpm is not predicted with any aerodynamic model.

6. Stability data obtained at 425 rpm compare well with whirl-tower data for low thrust levels. However, there are no whirl-tower data with which to compare data obtained at high thrust levels.

7. In comparing BO-105 damping data directly with data from a bearingless main rotor system, trends at constant rotational speed with varying thrust are similar. However, despite being more stable at design hovering conditions (425 rpm, $C_T/\sigma = 0.068$), the bearingless main rotor inplane operation is significantly less damped than is the BO-105 rotor system.

REFERENCES

1. Peterson, R. L.; and Warmbrodt, W.: Hover Test of a Full-Scale Hingeless Helicopter Rotor: Aeroelastic Stability, Performance and Loads Data. NASA TM-85892, 1984.

2. Johnson, W.: A Comprehensive Analytical Model of Rotorcraft Aerodynamics and Dynamics. NASA TM-81182, 1980.

3. Kloppel, V.; Kampa, K.; and Isselhorst, B.: Aeromechanical Aspects in the Design of Hingeless/Bearingless Rotor Systems. Paper No. 57, Ninth European Rotorcraft Forum, Stresa, Italy, Sept. 1983.

4. Warmbrodt, W.; and McCloud, J. L.: A Full-Scale Wind Tunnel Investigation of a Helicopter Bearingless Main Rotor. NASA TM-81321, 1981.

5. Staley, J. A.: Validation of Rotorcraft Flight Simulation Program through Correlation with Flight Data for Soft In-Plane Hingeless Rotors. USAAMRDL TR-75-50, Jan. 1976.

6. Landgrebe, Anton J.: The Wake Geometry of a Hovering Helicopter Rotor and Its Influence on Rotor Performance. J. Amer. Helicopter Soc., vol. 17, no. 4, Oct. 1972.

7. Kocurek, J. David; and Tangler, James L.: A Prescribed Wake Lifting Surface Hover Performance Analysis. J. Amer. Helicopter Soc., vol. 22, no. 1, Jan. 1977.

8. Peterson, R. L.; Warmbrodt, W.; and Hoover, J.: Aeromechanical Stability of a Full-Scale Hingeless Rotor in Hover. Paper No. A-84-40-62-3000, 40th Annual National Forum at the American Helicopter Society, Arlington, Va., May 1984.

1. Report No. NASA TM-85990	2. Government Accession No.	3. Recipient's Catalog No.
4. Title and Subtitle HOVER TEST OF A FULL-SCALE HINGELESS ROTOR		5. Report Date August 1984
		6. Performing Organization Code
7. Author(s) William Warmbrodt and Randall L. Peterson		8. Performing Organization Report No. A-9827
9. Performing Organization Name and Address Ames Research Center Moffett Field, CA 94035		10. Work Unit No. T-3504
		11. Contract or Grant No.
12. Sponsoring Agency Name and Address National Aeronautics and Space Administration Washington, DC 20546		13. Type of Report and Period Covered Technical Memorandum
		14. Sponsoring Agency Code 532-06-11

15. Supplementary Notes

Point of Contact: William Warmbrodt, Ames Research Center, MS 247-1,
Moffett Field, CA 94035   (415) 965-5642 or FTS 448-5642

16. Abstract

The performance and aeroelastic stability in hover of a 9.8-m diameter, hingeless helicopter rotor system was evaluated. Rotor performance and inplane damping data were obtained for rotor operation between 350 and 425 rpm for thrust coefficients (C_T/σ) between 0.0 and 0.12. At constant rotor thrust, a minimum in rotor inplane damping was measured at 400 rpm; the effect of experimental data scatter on this damping trend was determined to be insignificant. Good agreement is shown between experimental performance data and performance predicted by a comprehensive computer code. The influence of different aerodynamic inflow models on predicting damping levels is also shown. The best correlation with experimental stability data was obtained when a dynamic inflow model was used instead of static or quasi-static inflow models. Comparison with other full-scale, hingeless rotor data in hover is presented. Direct comparisons were also made between the hingeless rotor data and data from a full-scale, bearingless main rotor test performed on the same general-purpose test apparatus. The aerodynamic efficiency of the bearingless rotor was less at low thrust conditions, but was the same at design thrust. Although the bearingless rotor was more highly damped at design tip speed and 1-g thrust operation, greater sensitivity to operating conditions was shown. At low thrust levels the bearingless main rotor was less damped than the hingeless rotor.

17. Key Words (Suggested by Author(s)) Helicopters Rotary wing Rotor aerodynamics Ground resonance	18. Distribution Statement Unlimited Subject Category — 05

19. Security Classif. (of this report) Unclassified	20. Security Classif. (of this page) Unclassified	21. No. of Pages 23	22. Price* A02